Editors' Suggestion

Skyrmion-Based Programmable Logic Device with Complete Boolean Logic Functions

Z.R. Yan,[1,2] Y.Z. Liu,[1,2] Y. Guang,[1,2] K. Yue,[3] J.F. Feng,[1,2] R.K. Lake,[4] G.Q. Yu,[1,2,5,*] and X.F. Han[1,2,5,†]

[1] *Beijing National Laboratory for Condensed Matter Physics, Institute of Physics, Chinese Academy of Sciences, Beijing 100190, China*

[2] *Center of Materials Science and Optoelectronics Engineering, University of Chinese Academy of Sciences, Beijing 100049, China*

[3] *Ming Hsieh Department of Electrical and Computer Engineering, University of Southern California, Los Angeles, California 90089, USA*

[4] *Department of Electrical and Computer Engineering, University of California, Riverside, California 92521, USA*

[5] *Songshan Lake Materials Laboratory, Dongguan, Guangdong 523808, China*

(Received 4 February 2021; accepted 7 May 2021; published 2 June 2021)

A skyrmionic programmable logic device (SPLD) with complete Boolean logic functions is proposed and analyzed by micromagnetic simulations. The SPLD is based on an antiferromagnet-ferromagnet bilayer structure, in which the antiferromagnetic layer supports the interfacial Dzyaloshinskii-Moriya interaction and the out-of-plane exchange-bias field for stabilizing a zero-field skyrmion. By varying the local exchange-bias field, artificial pinning sites are introduced to trap skyrmions. Depending on the input currents and initial position of skyrmions at different pinning sites, different logic functions can be realized. Micromagnetic simulations show that the proposed SPLD has a robust performance, even under thermal fluctuations and inhomogeneity effects. Our work can provide insights for the design of programmable spin-logic devices.

DOI: 10.1103/PhysRevApplied.15.064004

I. INTRODUCTION

Magnetic order that can be harnessed via a magnetic field or electrical current is widely explored for memory, logic, and sensor applications [1–5]. The demand for scaling down the size of magnetic devices grows with developments in information processing and storage technologies. To this end, nanosized magnetic textures have been extensively studied with promising prospects on dense magnetic devices. A magnetic skyrmion is a newly discovered topological magnetic texture, which has received much attention due to its prominent properties, such as nanoscale size, nontrivial topology, and low driving current density [5–10]. These properties lead to proposals for a range of prototypes of skyrmionic devices, such as skyrmion racetrack memory [5,8,10–12] and skyrmion logic [13–17].

Boolean logic devices comprise the basic elements in modern electronic circuits. Conventional logic devices can be classified into two broad categories: a fixed logic device (FLD) and a programmable logic device (PLD) [18]. In recent years, many FLDs that are based on magnetic devices have been proposed. For example, a single magnetic domain, domain wall, or skyrmion can be employed as information bits to achieve different logic functionalities in FLD [13–17,19–26]. However, the logic functionality of the FLD is fixed once it has been manufactured, which limits flexibility in applications. In contrast, a PLD can be reconfigured and, hence, possesses multiple functionalities. Nonetheless, there are only a few research works reporting the realization of a skyrmion-based PLD [16]. Similar to the racetrack device, in a skyrmionic programmable logic device (SPLD), the input and output binary data bits "1" and "0" are encoded by the state with and without a skyrmion, respectively. Based on the voltage-controlled magnetic anisotropy effect, some SPLDs have been proposed [16,17]. However, racetrack-based devices may suffer from the skyrmion Hall effect (SKRHE), thermal fluctuations, and edge roughness, especially in constricted devices [7,12,27–31].

Here, we report a SPLD with complete Boolean logic functions (16 functions, including AND, NAND, XOR, etc.) based on artificially induced skyrmion pinning sites and current-driven skyrmion motion. Depending on the initial skyrmion position and applied currents, full logic

*guoqiangyu@iphy.ac.cn
†xfhan@iphy.ac.cn

functionalities can be achieved. The proposed scheme does not suffer from the SKRHE and skyrmion-edge repulsion, since the working principle does not involve long-range skyrmion diffusion and skyrmion-edge interactions. Furthermore, simulations with thermal fluctuations and inhomogeneity effects also demonstrate the robustness of the proposed SPLD device.

II. MODEL AND METHOD

The proposed logic device is shown in Fig. 1(a). The antiferromagnet (AFM)-based heterostructure is patterned into a crossbar with a center region of 400×450 nm^2. The antiferromagnetic layer provides the interfacial Dzyaloshinskii-Moriya interaction (DMI) and an exchange-bias field to the ferromagnetic (FM) layer, which endows zero-field stability to the skyrmion. Electrical currents are designed as input signals with identical amplitude, I_1 and I_2, which are orthogonal to each other. Due to the spin Hall effect in the AFM layer [32–37], the applied current generates spin-orbit torque and drives skyrmion motion in the FM layer [8,38,39]. To achieve different logic functions, the skyrmions must be initialized in the ferromagnetic layer by injecting a spin-polarized current through four different magnetic tunnel junctions (MTJs) marked as *A*, *B*, *C*, and *D*. MTJ *D* is also used to read the skyrmion as an output signal via the tunneling magnetoresistance (TMR) [9,10]. As shown in Figs. 1(b) and 1(c), the FM layer that hosts the skyrmions serves as the free layer of the MTJ, and the TMR is determined by the relative magnetization state between the FM layer and the fixed layer of the MTJ. The presence (absence) of a skyrmion can be defined as the high- (low-) resistance state. The local exchange-bias field can be manipulated by scanning-tip-based field cooling [40], x-ray exposure [41], or an electron beam to achieve effective pinning for the skyrmion [42]. Figure 1(d) shows the layout of pinning sites and MTJs. These pinning sites are designed for positioning the skyrmions. The input currents determine the direction of skyrmion motion associated with the SKRHE [7,30,31]. In the proposed device, we set the skyrmion Hall angle (θ_{SKRHE}) to about 45° for clarity, and this parameter can be optimized for different materials. Figures 1(e)–1(h) show the direction of skyrmion motion under different input current schemes. The influence of different θ_{SKRHE} values will be discussed later.

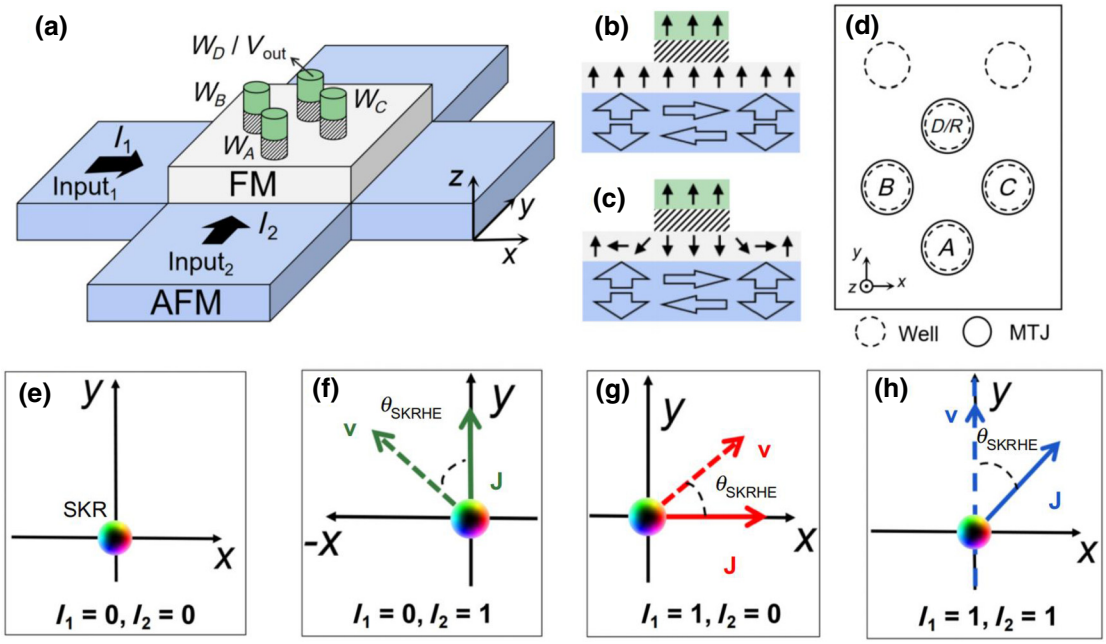

FIG. 1. Setup of device and motion of skyrmions under input current. (a) Illustration of the device configuration in FM-AFM bilayer. AFM layer (blue) is patterned into cross-shaped Hall bar, and FM layer (gray) cover the center region. Two orthogonal currents with identical amplitude, I_1 and I_2, are injected into AFM layer as input signals. Four magnetic tunnel junctions (MTJs), marked as *A*, *B*, *C*, and *D*, are used for writing skyrmions. MTJ *D* is also used for reading output voltage. (b),(c) Spin structures in MTJ of parallel (P) and antiparallel (AP) states, respectively. Spins in AFM layer are reoriented into local in-plane order, resulting in local exchange-bias field and pinning sites (PSs). (d) Layout of pinning sites and MTJs. (e)–(h) Skyrmion motion in FM layer under different input currents. **J** represents overall current direction, and **v** represents skyrmion velocity. $I_1 = 0$ and $I_2 = 0$ indicate no input current (or equivalently, input 0), leading to no skyrmion motion. $I_1 = 0$ ($I_1 = 1$) and $I_2 = 1$ ($I_2 = 0$) indicate applied in-plane current flowing along y (x) axis and skyrmion moving along vector $(-1, 1)$ [$(1, 1)$]. $I_1 = 1$ and $I_2 = 1$ indicate current flow along vector $(1, 1)$ and skyrmion moving along y axis.

To simulate skyrmion motion and design a skyrmionic programmable logic device, the micromagnetic simulation package Mumax3 is employed [43]. In the simulation, the magnetic system is discretized into a mesh of dimensions $1 \times 1 \times 1$ nm^3. The material-related parameters are as follows: saturation magnetization (M_S), 1.0×10^6 A/m; exchange stiffness constant (A), 1.5×10^{-11} J/m; Dzyaloshinskii-Moriya constant (D), 2 mJ/m^2; perpendicular magnetic anisotropy (PMA) constant (K_u), 0.9×10^6 J/m^3; spin Hall angle (θ_{SHE}), 0.4; and damping coefficient (α), 0.3. The dipole-dipole interaction is also considered. The working principle of the proposed device is irrespective of the edge and, hence, we do not consider the edge effect. The periodic boundary condition is adopted to improve the simulation efficiency (for more details of simulations with larger areas and open boundary conditions, see Appendix B). The pinning site induced by the local exchange-bias field (LEBF) serves as an effective potential well for the skyrmion. Such a pinning effect has been systematically investigated in our previous work [12]. It is shown that the pinning strength can be engineered by the size of the potential well (D_E) and the intensity of the exchange-bias field (H_E). For large D_E and H_E, the pinning effect is strong and the skyrmion is easily trapped by the pinning site. In our model, D_E is 60 nm and the nearest distance between different pinning sites is $240/\sqrt{2}$ nm. The effective local exchange-bias field, H_E, in the circle is 0.02 T (field direction along the y axis because the Néel orders are reconfigured by local thermal excitations induced by x-ray exposure [41] or an electron beam [42] and finally point to the $+y$ direction), while H_E outside the circular pinning region is 0.02 T (field direction along the z axis because the Néel orders in the AFM layer are initially uniformly pointing to the $+z$ direction). We consider a layered AFM and assume that the LEBF is not affected by magnetization dynamics in FM layer [41,42]. Thermal fluctuations (~300 K) are included. The effect of inhomogeneity is introduced by a 5% variation of saturation magnetization, exchange stiffness constant, DMI constant, and anisotropy in different grains (grain size approximately10 nm).

III. SKYRMION-BASED PROGRAMMABLE LOGIC GATES

We first explain the working principle of the logic operation for a XOR gate as an example. As shown in Fig. 2(a1), the clean operation is first executed by applying a large current pulse (~10^{12} A/m^2) to annihilate skyrmions on all MTJ sites. This operation can wipe out previously configured functions. To initialize the XOR function, two skyrmions are created at positions B and C by local injection of a spin-polarized current [Fig. 2(a2)]. Then, electric current pulses with duration $t_p = 3$ ns and density $J_p = 2 \times 10^{11}$ A/m^2 are injected as inputs. For the case with input signal $I_1 = 0$ and $I_2 = 0$ [Fig. 2(a3)], no electric current is injected and the skyrmions stay in their original position. Therefore, a low-resistance state in MTJ D is read out, showing an output signal of "$R = 0$," as shown in Fig. 2(a4). Figures 2(b1), 2(c1), and 2(d1) show the results for different combinations of input signals. If the input signal is $I_1 = 0$ ($I_1 = 1$) and $I_2 = 1$ ($I_2 = 0$), as shown in Fig. 1(b3) [Fig. 1(c3)], the applied in-plane current flows along the y (x) axis, and the skyrmions both move along the vector $(-1, 1)$ [$(1, 1)$]. After injection of the input current pulse, the skyrmion in the B (C) site moves to the D site. Finally, the high-resistance state in MTJ D is read out, showing an output signal of "$R = 1$" [Figs. 2(b4) and 2(c4)]. As for the case with $I_1 = 1$ and $I_2 = 1$, which is similar to the case of $I_1 = 0$ and $I_2 = 0$, no skyrmion moves into the D site, as a result $R = 0$ [Fig. 2(d4)].

In Fig. 3, we show the simulation results for several other logic gates. Different initial skyrmion configurations correspond to different logic operations. For example, initializing skyrmions at B and C sites leads to the function of the XOR logic gate, as discussed above. The initialization of skyrmions at sites A, D, AD, BC, ABC, and BCD leads to AND, NOR, NXOR, XOR, OR, and NAND logic gates, respectively. It should be noted that the device also has a stable performance under thermal fluctuations (300 K) and inhomogeneity effects. The proposed device can realize 16 logic functions (see Table I), including material implication [B for inverse implication (NIMP), C for reverse-inverse implication (RNIMP), ACD for inverse implication (IMP), and ABD for reverse implication (RIMP)], inoperation (AB for I_1 and AC for I_2), NOT gate (BD for NOT I_2 and CD for NOT I_1), false (no skyrmion set), and true ($ABCD$).

IV. DISCUSSION

A. Influences of θ_{SKRHE} and θ_{SHE}

The examples discussed above show that the skyrmion-shift operation determines the output signal, indicating that the logic operation relies on stable skyrmion positioning and precise skyrmion-shift operation. Thus, θ_{SKRHE} is an important parameter in this device. For specific values of θ_{SKRHE}, the design of the layout of pinning sites and MTJs should be further optimized, as shown in Appendix A [Figs. 5(d), 5(h), and 6]. On the other hand, θ_{SHE} also influences the amplitude and duration of the input current pulse and is closely related to the operation frequency.

To further understand the role of θ_{SHE} and the magnitude of the input current pulse J_p, we employ Thiele's approach [8,38,39]. Their relationship can be obtained from the Thiele equation:

$$\vec{G} \times \vec{v} - \alpha \overleftrightarrow{D} \cdot \vec{v} + 4\pi B \overleftrightarrow{R} \cdot \vec{J} = 0. \tag{1}$$

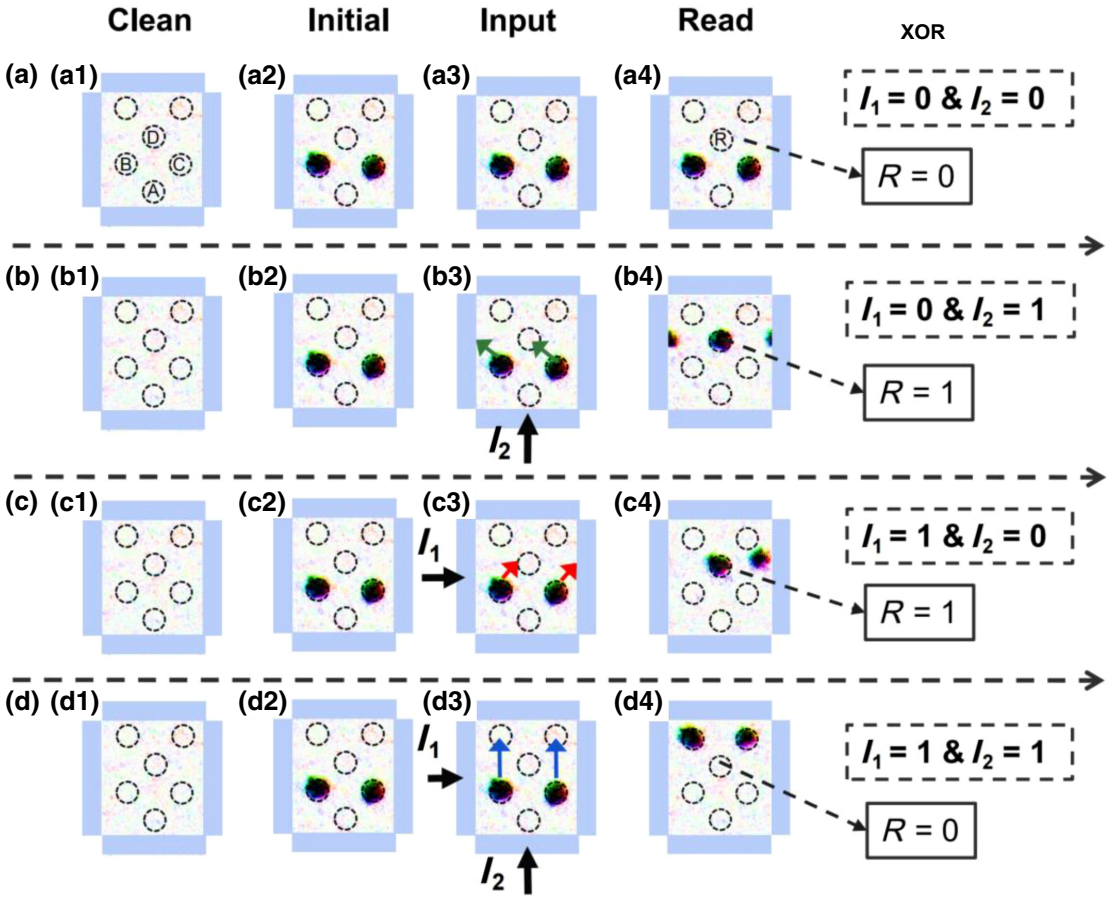

FIG. 2. Simulated logic device with XOR function. Complete process includes four sets of inputs, (a) $I_1 = 0$ and $I_2 = 0$, (b) $I_1 = 0$ and $I_2 = 1$, (c) $I_1 = 1$ and $I_2 = 0$, (d) $I_1 = 1$ and $I_2 = 1$, and four operations, clean, initialization (initial for short), input, and read. (a1)–(d1) "Clean" operation wipes out all skyrmions in FM layers by using a large current pulse. (a2)–(d2) "Initialization" operation creates skyrmions in specified pinning sites to initialize specific logic function. (a3)–(d3) "Input" operation injects input signals (currents) and drives skyrmion motion. Black arrows indicate input currents. Arrows in green, red, and blue show the trajectory of skyrmions after injecting current. (a4)–(d4) "Read" operation reads output voltage signal from MTJ *D*. Output signals, *R*, are indicated by dashed arrows.

Here, $\vec{G} = (0,\ 0,\ g)$ is gyrocoupling vector with $g = 4\pi$, $\vec{v} = (v_x,\ v_y)$ is the velocity of the skyrmion, and $\vec{J} = (J_p,\ 0)$ is the current density. $\overleftrightarrow{D} = \begin{bmatrix} D_0 & 0 \\ 0 & D_0 \end{bmatrix}$ is the dissipative tensor, and $\overleftrightarrow{R} = \begin{bmatrix} \cos\varphi_0 & \sin\varphi_0 \\ -\sin\varphi_0 & \cos\varphi_0 \end{bmatrix}$ is an in-plane rotation matrix with $\varphi_0 = 0$ for the Néel skyrmion. α is the Gilbert damping and coefficient $B = [(\gamma_0 \hbar \theta_{\mathrm{SHE}} L_{\mathrm{sc}} I_\rho)/(2eM_s L)]$ is linked to the spin Hall effect, where γ_0 the gyromagnetic ratio, $\hbar$ is the reduced Planck constant, θ_{SHE} is the spin Hall angle, e is the electron charge, M_s is the saturation magnetization, L is the thickness of the ferromagnetic layer, L_{sc} is the scaling length equal to the strip width, and I_ρ is the shape factor of the skyrmion.

The solution of Eq. (1) is given (without boundary conditions) as

$$\begin{aligned} -gv_y - \alpha D_0 v_x + 4\pi B J_p &= 0, \\ gv_x - \alpha D_0 v_y &= 0. \end{aligned} \tag{2}$$

Then, we can obtain the relationship between the velocity of the skyrmion and the input current pulse:

$$v = \sqrt{v_x^2 + v_y^2} = \frac{4\pi B J_p}{\sqrt{\alpha^2 D_0^2 + g^2}}. \tag{3}$$

Therefore, the shift of the skyrmion between nearest pinning sites can be described as

$$S = v t_p, \tag{4}$$

where S is the distance between the nearest pinning sites and t_p is the duration of input current pulse. From Eqs. (3) and (4), one obtains

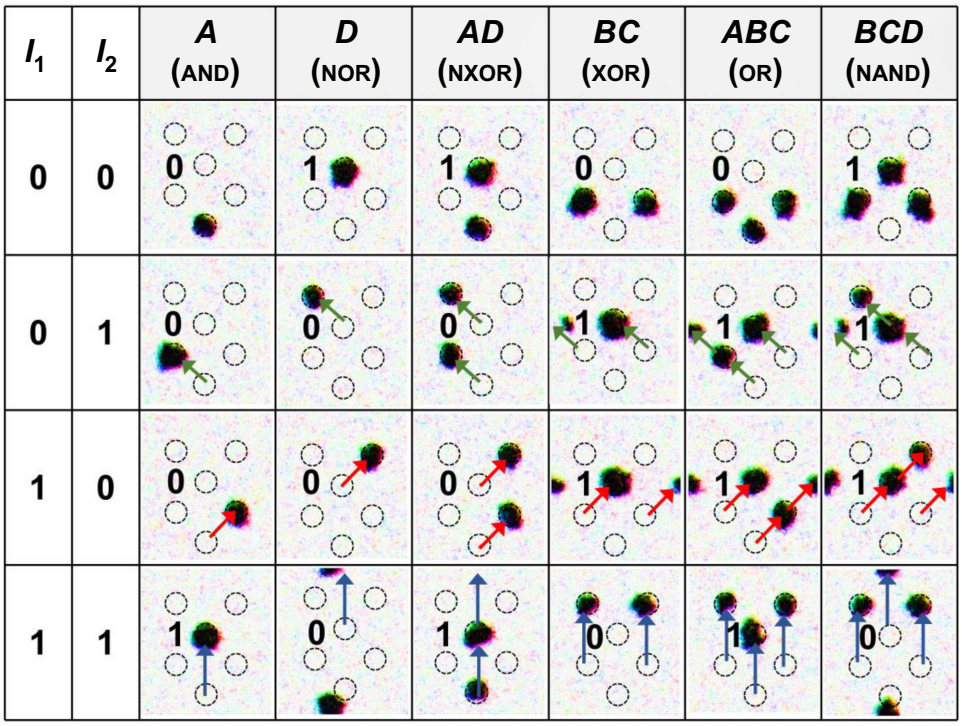

FIG. 3. Simulated results of different logic functions. Function is configured by setting skyrmions in specified pinning sites. Corresponding initial states and logic functions (written in brackets) are shown in the first row. 1" and 0 indicate output signals from MTJ *D*. Arrows in green, red, and blue show trajectory of skyrmions after injecting different input currents.

$$t_p J_p \theta_{\mathrm{SHE}} = C, \tag{5}$$

where $C = SeM_s L\sqrt{\alpha^2 D_0^2 + g^2}/2\pi\gamma_0\hbar I_\rho L_{\mathrm{sc}}$ is a constant for a given device. In our system, for $t_p = 3$ ns, $J_p = 2 \times 10^{11}$ A/m^2, and $\theta_{\mathrm{SHE}} = 0.4$, $C = 1.2 \times 10^{11}$ ns A/m^2 is obtained. The relationship between t_p and J_p is shown in Fig. 4. It is obvious that t_p is inversely proportional to J_p. As mentioned above, large D_E and H_E lead to a relatively strong pinning effect. Although the LEBF potential well can pin the skyrmion, it also causes a problem when driving the skyrmion. Thus, J_p should be larger than the

TABLE I. Sixteen logic functions programmed by different skyrmion configurations. Gray cells indicate input values (I_1 and I_2). Corresponding initial states for different logic functions (written in brackets) are shown in the first row. Orange cells represent common logic functions. Blue cells indicate material implication. Green cells indicate inoperations and a NOT gate. Pink cells represent false and true.

I_1	I_2	A(AND)	B(NIMP)	C(RNIMP)	D(NOR)	AB(I_1)	AC(I_2)	AD(NXOR)	BC(XOR)
0	0	0	0	0	1	0	0	1	0
0	1	0	0	1	0	0	1	0	1
1	0	0	1	0	0	1	0	0	1
1	1	1	0	0	0	1	1	1	0

I_1	I_2	BD(NOT I_2)	CD(NOT I_1)	ABC(OR)	BCD(NAND)	ACD(IMP)	ABD(RIMP)	--(False)	ABCD(True)
0	0	1	1	0	1	1	1	0	1
0	1	0	1	1	1	1	0	0	1
1	0	1	0	1	1	0	1	0	1
1	1	0	0	1	0	1	1	0	1

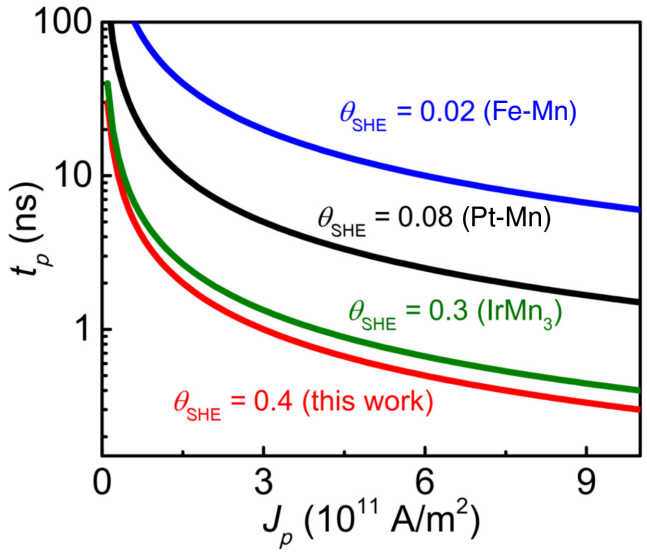

FIG. 4. Duration of input current (t_p) as a function of current amplitude (J_p) for various θ_{SHE}. Curves are plotted according to Eq. (6) with different values of θ_{SHE} marked by blue 0.02 for Fe-Mn [49], green (0.3 for $IrMn_3$ [35]), and black (0.08 for Pt-Mn [34]).

critical driving current (J_c) to overcome the trapping force and drive the skyrmion out of the LEBF potential well. The influence of D_E and H_E on J_c are similar to that of pinning strength. Therefore, D_E and H_E need to be engineered to obtain optimal J_c and J_p [12]. The spin Hall angle also plays an important role in the device. Antiferromagnets with large spin Hall angles, such as $IrMn_3$ [35] or Pt-Mn [34], are expected to increase the speed and energy efficiency of the device.

To build a robust device with high performance and energy efficiency, an antiferromagnetic metal with a large spin-orbit coupling (providing large enough values of DMI and θ_{SKRHE}) and exchange-bias effects at room temperature is necessary. This specific requirement limits the variety of alternative materials. $IrMn_3$ and Pt-Mn are promising candidates for the antiferromagnetic layer, but other antiferromagnets can also be explored. On the other hand, the initialization of skyrmions leads to extra energy consumption and longer operating time, which need to be optimized. One solution is to increase the spin polarization of the electric current to lower the critical current for writing of the skyrmions. The dipolar field originating from the fixed layer of MTJ is neglected in our simulation for simplicity, but for sub-100-nm MTJ the dipolar field may affect the pinning strength and needs to be further modified [12]. By using an optimized MTJ structure, the energy consumption of the initialization operation can be greatly reduced [44]. It is also possible to employ the electric-field-assisted method to further optimize the device [45].

B. More inputs of instructions

For a programmable logic device, additional inputs of instructions are needed for more functions. In general, the number of logic functions (N_F) is determined by the number of instructions (N_{ins}). For binary instruction, a device with 16 complete logic functions needs four additional inputs of instructions. The four terminals in our proposal correspond to the four MTJs (at the *A*, *B*, *C*, and *D* sites). For other types of magnetic logic device [13,46–48], it is found that more terminals of instructions lead to more functions, indicating the importance of N_{ins}. Such multi-instruction schemes can also be implemented in logic devices based on other physical systems, providing a guideline for the design of a programmable logic device with multiple functions.

V. CONCLUSION

We propose a skyrmionic programmable logic device that includes 16 types of logic functions. The logic functions are configured by initializing the layout of skyrmions. The pinning sites can enhance the stability and certainty of skyrmion motion, and the device thus shows significant robustness under the effect of inhomogeneity and thermal fluctuations. Our work could stimulate the design of a PLD with complete functions and serve as a candidate for future skyrmionic logic applications.

ACKNOWLEDGMENTS

This work is funded by the National Key Research and Development Program of China (Grant No. 2017YFA0206200), the Science Center of the National Science Foundation of China (Grant No. 52088101), the National Natural Science Foundation of China (NSFC, Grants No. 11874409 and No. 11804380), the Beijing Natural Science Foundation (Grant No. Z190009), the NSFC-Science Foundation Ireland (SFI) Partnership Programme (Grant No. 51861135104), and the K. C. Wong Education Foundation (Grant No. GJTD-2019-14). Y.L. also acknowledges support from the Institute of Physics, Chinese Academy of Sciences, through an International Young Scientist Fellowship (Grant No. 2018001). R.K.L. acknowledges support from Spins and Heat in Nanoscale Electronic Systems (SHINES), an Energy Frontier Research Center funded by the U.S. Department of Energy, Office of Science, Basic Energy Sciences under Award No. DE-SC0012670.

APPENDIX A: LAYOUT OF PINNING SITES AND MTJS

The skyrmion Hall angle determines the direction of motion of the skyrmion under an applied current. This machine thus influences the layout of pinning sites and

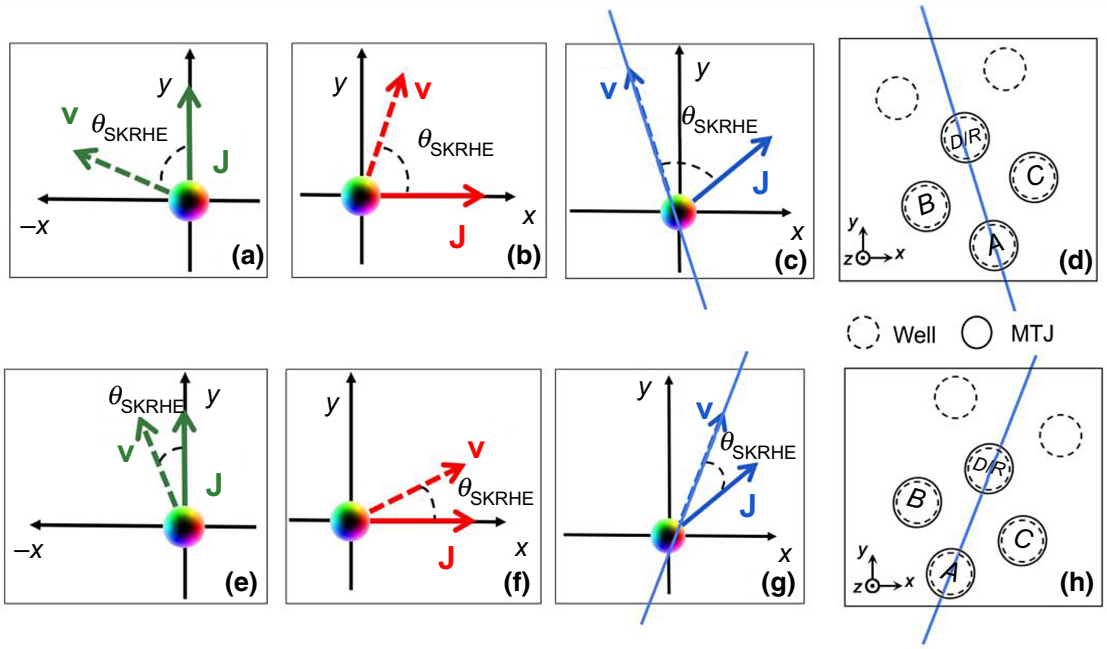

FIG. 5. Sketch of the layout of pinning sites and MTJs in different skyrmion Hall angle. (a)–(c),(e)–(g) Skyrmion motion with small and large skyrmion Hall angles, respectively. (d),(h) Layouts of pinning sites and MTJs. Solid blue lines in (c),(g) are parallel to those in (d),(h).

MTJs in the proposed skyrmionic programmable logic device, as shown in Figs. 5(d) and 5(h). For $\theta_{SKRHE} \approx 45°$, the layout is shown in Fig. 1(d). For $\theta_{SKRHE} > 45°$ ($\theta_{SKRHE} < 45°$), the layout can be obtained by complete counterclockwise (clockwise) rotation of the one at $\theta_{SKRHE} = 45°$. For example, when the damping constant is 0.01, the skyrmion Hall angle is close to 90°. Thus, the layout of the device is rotated about 45° clockwise. The simulation results are shown in Fig. 6. The performance of the proposed device is still robust. This also implies that damping should be taken into account when optimizing the device.

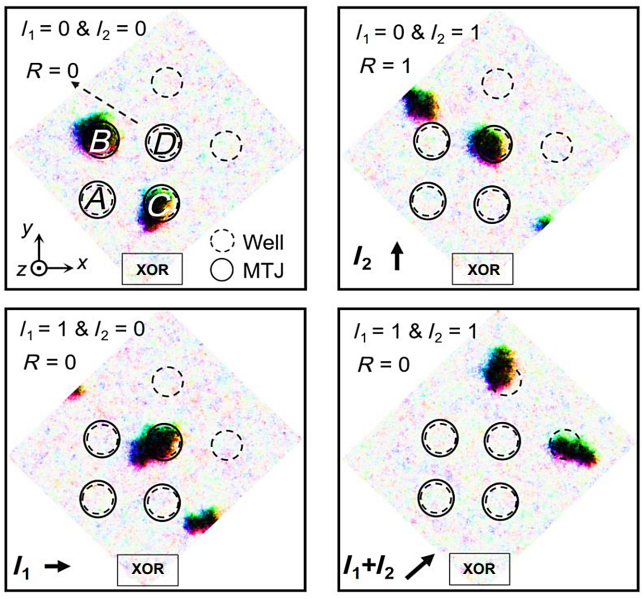

FIG. 6. Simulation results for XOR gate with damping $\alpha = 0.01$.

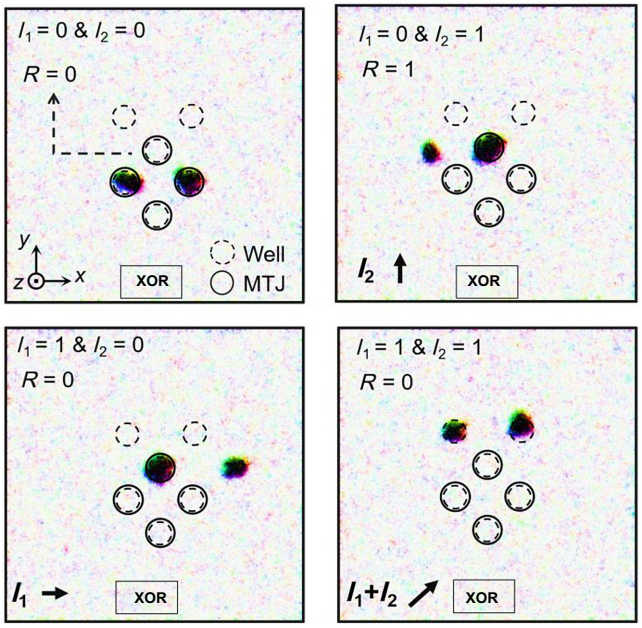

FIG. 7. Simulation results for XOR gate with sample size $800 \times 800 \times 1$ nm^3 under open boundary conditions.

APPENDIX B: MICROMAGNETIC SIMULATIONS WITH LARGE AREA AND OPEN BOUNDARY CONDITIONS

Figure 7 shows the simulation results of the XOR gate with sample size $800 \times 800 \times 1$ nm^3 and open boundary conditions. The results are still robust and similar to those shown in Fig. 2.

[1] A. Wang and W. D. Woo, Static magnetic storage and delay line, J. Appl. Phys. **21**, 49 (1950).

[2] M. Kestigian, A. B. Smith, and W. R. Bekebrede, Past, present and future small-bubble-diameter magnetic memory materials, J. Appl. Phys. **50**, 2161 (1979).

[3] G. Y. Chin, New magnetic alloys, Science **208**, 888 (1980).

[4] S. S. P. Parkin, M. Hayashi, and L. Thomas, Magnetic domain-wall racetrack memory, Science **320**, 190 (2008).

[5] A. Fert, V. Cros, and J. Sampaio, Skyrmions on the track, Nat. Nanotech. **8**, 152 (2013).

[6] N. Nagaosa and Y. Tokura, Topological properties and dynamics of magnetic skyrmions, Nat. Nanotech. **8**, 899 (2013).

[7] J. Sampaio, V. Cros, S. Rohart, A. Thiaville, and A. Fert, Nucleation, stability and current-induced motion of isolated magnetic skyrmions in nanostructures, Nat. Nanotech. **8**, 839 (2013).

[8] R. Tomasello, E. Martinez, R. Zivieri, L. Torres, M. Carpentieri, and G. Finocchio, A strategy for the design of skyrmion racetrack memories, Sci. Rep. **4**, 6784 (2014).

[9] R. Wiesendanger, Nanoscale magnetic skyrmions in metallic films and multilayers: A new twist for spintronics, Nat. Rev. Mater. **1**, 16044 (2016).

[10] A. Fert, N. Reyren, and V. Cros, Magnetic skyrmions: Advances in physics and potential applications, Nat. Rev. Mater. **2**, 17031 (2017).

[11] G. Yu, P. Upadhyaya, Q. Shao, H. Wu, G. Yin, X. Li, C. He, W. Jiang, X. Han, P. K. Amiri, and K. L. Wang, Room-temperature skyrmion shift device for memory application, Nano Lett. **17**, 261 (2017).

[12] Z. R. Yan, Y. Z. Liu, Y. Guang, J. F. Feng, R. K. Lake, G. Q. Yu, and X. F. Han, Robust Skyrmion Shift Device Through Engineering the Local Exchange-Bias Field, Phys. Rev. Appl. **14**, 044008 (2020).

[13] X. Zhang, M. Ezawa, and Y. Zhou, Magnetic skyrmion logic gates: Conversion, duplication and merging of skyrmions, Sci. Rep. **5**, 9400 (2015).

[14] X. Xing, P. W. T. Pong, and Y. Zhou, Skyrmion domain wall collision and domain wall-gated skyrmion logic, Phys. Rev. B **94**, 054408 (2016).

[15] Z. He, S. Angizi, and D. Fan, Current-induced dynamics of multiple skyrmions with domain-wall pair and skyrmion-based majority gate design, IEEE Magnetics Letters **8**, 1 (2017).

[16] S. Luo, M. Song, X. Li, Y. Zhang, J. Hong, X. Yang, X. Zou, N. Xu, and L. You, Reconfigurable skyrmion logic gates, Nano Lett. **18**, 1180 (2018).

[17] H. Yang, C. Wang, X. Wang, X. S. Wang, Y. Cao, and P. Yan, Twisted skyrmions at domain boundaries and the method of image skyrmions, Phys. Rev. B **98**, 014433 (2018).

[18] K. Skahill, *VHDL for Programmable Logic* (Addison-Wesley Longman Publishing Co., Inc., Redwood City, 1996).

[19] D. A. Allwood, G. Xiong, C. C. Faulkner, D. Atkinson, D. Petit, and R. P. Cowburn, Magnetic domain-wall logic, Science **309**, 1688 (2005).

[20] M. P. Kostylev, A. A. Serga, T. Schneider, B. Leven, and B. Hillebrands, Spin-wave logical gates, Appl. Phys. Lett. **87**, 153501 (2005).

[21] P. Xu, K. Xia, C. Gu, L. Tang, H. Yang, and J. Li, An all-metallic logic gate based on current-driven domain wall motion, Nat. Nanotech. **3**, 97 (2008).

[22] K. A. Omari and T. J. Hayward, Chirality-Based Vortex Domain-Wall Logic Gates, Phys. Rev. Appl. **2**, 044001 (2014).

[23] A. V. Chumak, V. I. Vasyuchka, A. A. Serga, and B. Hillebrands, Magnon spintronics, Nat. Phys. **11**, 453 (2015).

[24] T. Schneider, A. A. Serga, B. Leven, B. Hillebrands, R. L. Stamps, and M. P. Kostylev, Realization of spin-wave logic gates, Appl. Phys. Lett. **92**, 022505 (2008).

[25] T. Liu and G. Vignale, Electric Control of Spin Currents and Spin-Wave Logic, Phys. Rev. Lett. **106**, 247203 (2011).

[26] K. Vogt, F. Y. Fradin, J. E. Pearson, T. Sebastian, S. D. Bader, B. Hillebrands, A. Hoffmann, and H. Schultheiss, Realization of a spin-wave multiplexer, Nat. Commun. **5**, 3727 (2014).

[27] R. Duine, Skyrmions singled out, Nat. Nanotech. **8**, 800 (2013).

[28] J. Iwasaki, M. Mochizuki, and N. Nagaosa, Current-induced skyrmion dynamics in constricted geometries, Nat. Nanotech. **8**, 742 (2013).

[29] X. Zhang, G. P. Zhao, H. Fangohr, J. P. Liu, W. X. Xia, J. Xia, and F. J. Morvan, Skyrmion-skyrmion and skyrmion-edge repulsions in skyrmion-based racetrack memory, Sci. Rep. **5**, 7643 (2015).

[30] W. Jiang, X. Zhang, G. Yu, W. Zhang, X. Wang, M. Benjamin Jungfleisch, John E. Pearson, X. Cheng, O. Heinonen, K. L. Wang, Y. Zhou, A. Hoffmann, and Suzanne G. E. te Velthuis, Direct observation of the skyrmion Hall effect, Nat. Phys. **13**, 162 (2016).

[31] K. Litzius, I. Lemesh, B. Krüger, P. Bassirian, L. Caretta, K. Richter, F. Büttner, K. Sato, O. A. Tretiakov, J. Förster, R. M. Reeve, M. Weigand, I. Bykova, H. Stoll, G. Schütz, G. S. D. Beach, and M. Kläui, Skyrmion Hall effect revealed by direct time-resolved X-ray microscopy, Nat. Phys. **13**, 170 (2016).

[32] J. B. S. Mendes, R. O. Cunha, O. Alves Santos, P. R. T. Ribeiro, F. L. A. Machado, R. L. Rodríguez-Suárez, A. Azevedo, and S. M. Rezende, Large inverse spin Hall effect in the antiferromagnetic metal $Ir_{20}Mn_{80}$, Phys. Rev. B **89**, 140406 (2014).

[33] V. Tshitoyan, C. Ciccarelli, A. P. Mihai, M. Ali, A. C. Irvine, T. A. Moore, T. Jungwirth, and A. J. Ferguson, Electrical manipulation of ferromagnetic NiFe by antiferromagnetic IrMn, Phys. Rev. B **92**, 214406 (2015).

[34] Y. Ou, S. Shi, D. C. Ralph, and R. A. Buhrman, Strong spin Hall effect in the antiferromagnet PtMn, Phys. Rev. B **93**, 220405 (2016).

[35] W. Zhang, W. Han, S.-H. Yang, Y. Sun, Y. Zhang, B. Yan, and S. S. P. Parkin, Giant facet-dependent spin-orbit torque and spin Hall conductivity in the triangular antiferromagnet $IrMn_3$, Sci. Adv. **2**, e1600759 (2016).

[36] G. Yu, A. Jenkins, X. Ma, S. A. Razavi, C. He, G. Yin, Q. Shao, Q. l. He, H. Wu, W. Li, W. Jiang, X. Han, X. Li, A. C. Bleszynski Jayich, P. K. Amiri, and K. L. Wang, Room-temperature skyrmions in an antiferromagnet-based heterostructure, Nano Lett. **18**, 980 (2018).

[37] D. Wu, G. Yu, C.-T. Chen, S. A. Razavi, Q. Shao, X. Li, B. Zhao, K. L. Wong, C. He, Z. Zhang, P. Khalili Amiri, and K. L. Wang, Spin-orbit torques in perpendicularly magnetized $Ir_{22}Mn_{78}/Co_{20}Fe_{60}B_{20}/MgO$ multilayer, Appl. Phys. Lett. **109**, 222401 (2016).

[38] A. A. Thiele, Steady-State Motion of Magnetic Domains, Phys. Rev. Lett. **30**, 230 (1973).

[39] S.-J. Lee, K.-W. Kim, H.-W. Lee, and K.-J. Lee, Spin-orbit-torque-induced skyrmion dynamics for different types of spin-orbit coupling, J. Magn. Magn. Mater. **455**, 14 (2018).

[40] E. Albisetti, D. Petti, M. Pancaldi, M. Madami, S. Tacchi, J. Curtis, W. P. King, A. Papp, G. Csaba, W. Porod, P. Vavassori, E. Riedo, and R. Bertacco, Nanopatterning reconfigurable magnetic landscapes via thermally assisted scanning probe lithography, Nat. Nanotech. **11**, 545 (2016).

[41] Y. Guang, et al., Creating zero-field skyrmions in exchange-biased multilayers through X-ray illumination, Nat. Commun. **11**, 949 (2020).

[42] Y. Guang, Y. Peng, Z. Yan, Y. Liu, J. Zhang, X. Zeng, S. Zhang, S. Zhang, D. M. Burn, and N. Jaouen, Electron beam lithography of magnetic skyrmions, Adv. Mater. **32**, 2003003 (2020).

[43] A. Vansteenkiste, J. Leliaert, M. Dvornik, M. Helsen, F. Garcia-Sanchez, and B. Van Waeyenberge, The design and verification of MuMax3, AIP Adv. **4**, 107133 (2014).

[44] X. Chen, H. Zhang, E. Deng, M. Yang, N. Lei, Y. Zhang, W. Kang, and W. Zhao, Sky-RAM: Skyrmionic random access memory, IEEE Electron Device Lett. **40**, 722 (2019).

[45] J.-M. Hu, Z. Li, L.-Q. Chen, and C.-W. Nan, High-density magnetoresistive random access memory operating at ultralow voltage at room temperature, Nat. Commun. **2**, 553 (2011).

[46] Z. Luo, A. Hrabec, T. P. Dao, G. Sala, S. Finizio, J. Feng, S. Mayr, J. Raabe, P. Gambardella, and L. J. Heyderman, Current-driven magnetic domain-wall logic, Nature **579**, 214 (2020).

[47] X. Zhang, C. H. Wan, Z. H. Yuan, C. Fang, W. J. Kong, H. Wu, Q. T. Zhang, B. S. Tao, and X. F. Han, Experimental demonstration of programmable multi-functional spin logic cell based on spin Hall effect, J. Magn. Magn. Mater. **428**, 401 (2017).

[48] W. Yu, J. Lan, and J. Xiao, Magnetic Logic Gate Based on Polarized Spin Waves, Phys. Rev. Appl. **13**, 024055 (2020).

[49] W. Zhang, *et al.*, All-electrical manipulation of magnetization dynamics in a ferromagnet by antiferromagnets with anisotropic spin Hall effects, Phys. Rev. B **92**, 144405 (2015).